Lasers in Manufacturing Conference 2023

Parameters optimization of Ti6Al4V alloy welding by pulsed Nd:YAG laser

Hana Chmelíčková [a,b,*], Martina Havelková[b], Aneta Hrubantová Písaříková [a,c], Vlastimil Jílek[a,b], Lukáš Václavek[a,b]

[a]*Palacký University Olomouc, Faculty of Science, Joint Laboratory of Optics of Palacký University and Institute of Physics AS CR, 17. listopadu 1192/12,Olomouc, 779 00, Czech Republic*
[b]*Institute of Physics of the Academy of Sciences of the Czech Republic, Joint Laboratory of Optics of Palacký University and Institute of Physics AS CR, 17. listopadu 1154/50A, Olomouc, 779 00, Czech Republic*
[c]*Institute of Physics of the Czech Academy of Sciences,Department of Low-Temperature Plasma, Na Slovance1999/ 2, Praha 8, 182 00, Czech Republic*

Abstract

The butt welds of thin Ti6Al4V alloy sheets using a pulsed Nd:YAG laser were investigated to determine the optimal value of peak power and pulse length for creating sound welds. The width of the weld face and the depth of penetration were found to be proportional to increasing peak power and decreasing pulse length. The weld surfaces were measured using a contact profilometer. The influence of laser pulse overlap on the thermal cycle in representative point and cross-section planes was demonstrated by a numerical model. Repeated melting and heating above the transformation temperature by previous and following pulses probably caused the occurrence of a mixed microstructure of α´martensite and massive α in the fusion zone and near the heat-affected zone. Nanohardness tests on the transverse cross-sections showed that the fusion zone was approximately 50% harder than the base material. X-ray diffraction analysis of the central parts of the welds confirmed the presence of coincidence peaks of α´martensite and α phase.

Keywords: Laser welding; Ti6Al4V; FEM model; Nanoindentation; XRD analysis

* Corresponding author. Tel.: +420-585-631-516; fax: +420-585-631-531.
E-mail address: hana.chmelickova@upol.cz

1. Introduction

Excellent physical properties – high specific strength, low density, high melting temperature, exceptional corrosion resistance, biocompatibility – predestine titanium and its alloys for use in extreme operating conditions (aerospace, automotive, petrochemical, and nuclear industry, or medicine), Kumar et al., 2018a. Laser welding of titanium alloy Ti6Al4V overcomes problems with the high heat input and extensive heat-affected zone in the case of the arc welding methods. Kabir et al., 2010 investigated CW Nd: YAG 4 kW laser welding of 5.1 mm thick plates with constant power and increasing welding speed in two defocusing positions. It was found, that width and area of the fusion and heat-affected zones inversely dependent on the welding speed. The CW Yb: disk laser was used to study the influence of laser processing parameters on the quality and mechanical properties of the 2 mm long butt welds, Lisiecki, 2012. Kumar et al., 2018b published a detailed study of CW Yb: fiber laser welding of 2 mm plates with an increasing set of heat inputs from 74 $J.mm^{-1}$ to 131 $J.mm^{-1}$. Comparison of the continual and pulsed welding modes was performed on 0.8 mm thin plates to investigate the difference in the microstructural morphology, Kumar et al., 2020. Laser welding includes many interrelated process parameters, which determine heat input, defined as the ratio of average power and scanning velocity. Pulsed laser welding is associated with 60% - 80% pulse overlap to ensure a tight joint, Chludzinski et al., 2021. It means, that more pulses impact the area of one laser spot. Previous pulses act as a preheating and partial melting factor, following ones cause partial re-melting and post-heating.

The objective of the present study is to investigate weld bead properties dependence on the increasing pulse peak power and decreasing pulse length simultaneously, while the pulse energy, average power, and heat input remained constant.

2. Materials and methods

Thin plates of the Ti6Al4V alloy with dimensions (150 x 40 x 0.8) mm^3 were welded in butt configuration by pulsed Nd: YAG laser KLS 246 – 102 150 W with fixed processing head containing 100 mm focusing lens. The workpiece support was mounted on the horizontal XY linear axis. Optimal focus offset +3 mm from specimen surface was found in previous experiments where theoretical beam diameter 0.84 mm is suitable for welding, Sibillano et al., 2012. Weld pool shielding was realized by argon guided through 2 mm nozzle at a flow rate 12 $l.min^{-1}$. Pulse frequency 13 Hz and scanning velocity 3 $mm.s^{-1}$ were set as constant parameters, calculated pulse overlap was then 72.5 %.

The influence of the increasing pulse energy within constant pulse length 3 ms on penetration depth was previously investigated with the CP titanium Gr.1 sheets of thickness 0.8 mm in range from 2.63 J to 5.58 J, Chmelíčková et al., 2020. Optimal pulse energy 5.03 J was now used to investigate the influence of the increasing pulse length with Ti6Al4V sheets. Pulse length was gradually set from 2 ms to 5.5 ms with 0.5 ms increment, pulse peak power consequently decreased from 2.515 kW to 0.915 kW. The average power 65.39 W and heat input 21.8 $J.mm^{-1}$ remained constant.

Weld dimensions on the transverse cross sections were measured by means of the laser scanning confocal microscope LEXT 5000 with objective 20x (magnification 480x). Digital microscope KEYENCE VHX-7100 was used for the microstructure evaluation in welds selected parts in Optical Shadow Effect Mode (magnification 2500x), which provides plastic view of the weld structure. Surface morphology of the top and bottom weld sides was examined by the contact profilometer TALYSURF in fifty points per millimeter at representative (4 x 4) mm^2 area. Connected software TALYMAP was used to create 2D and 3D surface visualisations.

Methodology developed for the pulsed laser welding in FEM software SYSWELD was applied besides steels also for Ti6Al4V, Lapšanská et al., 2010. Pulsed welding was simulated by the periodically time dependent intensity function, that acquired value 1 for time during pulse duration t_p and value 0 for the remaining time

to the next pulse beginning, which is equal to (0.076923 s – t_p) in the case of used frequency 13 Hz. Predefined 3D Gaussian conical heat source was defined by volume power density 3200 W.mm^{-3} and geometric parameters were set according to measured dimensions of the weld cross section. Temperature history both in the weld-line and representative point in the fusion zone centre and 2D temperature distribution in the weld cross sections were displayed through the Post-processing menu.

Mechanical properties of both fully penetrated and heat conduction shallow welds were determined by means of the nanoindentation tests on their transverse cross-sections with spacing 100 µm. The fully calibrated NanoTest instrument, (Micro Materials, UK) equipped with a diamond pyramidal Berkovich tip at a maximal load of 50 mN was used at room temperature. Nanohardness and reduced elastic modulus (E_r) values were calculated based on the analysis of nanoindentation curves via a standard Oliver-Pharr method.

XRD analysis of the optimal sample was realized by Empyrean diffractometer in Bragg-Brentano geometry with Cu Kα radiation (λ = 0.154 nm) in 2θ range 10° - 90° with a step size 0.053°. Measured XRD patterns were identified by HighScore Plus 4.0 software package (PANalytical), that uses data from the international database JCPDS - Joint Committee on Powder Diffraction Standards.

3. Results and discussion

3.1. Weld dimensions on the surface and the cross section

Weld dimensions dependence on the increasing pulse length and decreasing peak power is presented in Table 1. Weld face width has tendency to increase with peak power from (804 ± 15) µm to (1043 ± 44) µm. Root width of three fully penetrated welds apparently increased with distance from the weld start due to gradual heating of the material, (472 ± 43) µm for sample 2 and (441 ± 83) µm for sample 3, resp., width of the sample 1 extremely humped root is (661 ± 49) µm.

Table 1. Weld dimensions dependence on the increasing pulse length and the decreasing peak power

Sample	Pulse length (*ms*)	Peak power (*kW*)	Intensity (*kW.cm^{-2}*)	Face width (µ*m*)	Root width (µ*m*)	Axial depth (µ*m*)
1	2.0	2.515	454	677 ± 38	661 ± 49	-
2	2.5	2.012	363	1008 ± 55	472 ± 43	-
3	3.0	1.677	303	1043 ± 44	441 ± 83	-
4	3.5	1.429	259	1045 ± 25	-	789
5	4.0	1.258	227	974 ± 32	-	549
6	4.5	1.118	202	946 ± 13	-	364
7	5.0	1.006	182	867 ± 80	-	248
8	5.5	0.915	165	804 ± 15	-	194

The highest used peak power 2.515 kW caused expelling of the melt pool from the weld line and extreme melt dropout with a root humping 114 µm (sample 1), these values decreased in case of the peak power 1.677 kW to 87 µm and 36.7 µm, respectively (sample 3). Maximal depth of penetration 789 µm occurred at peak power 1.429 kW (sample 4). Lack of penetration 549 µm appears in case of the peak power 1.258 kW (sample 5), the next three samples 6, 7 and 8 were welded only by the heat conduction mode with shallow penetration depth from 364 µm, 248 µm and 194 µm in the sample center (Fig 1).

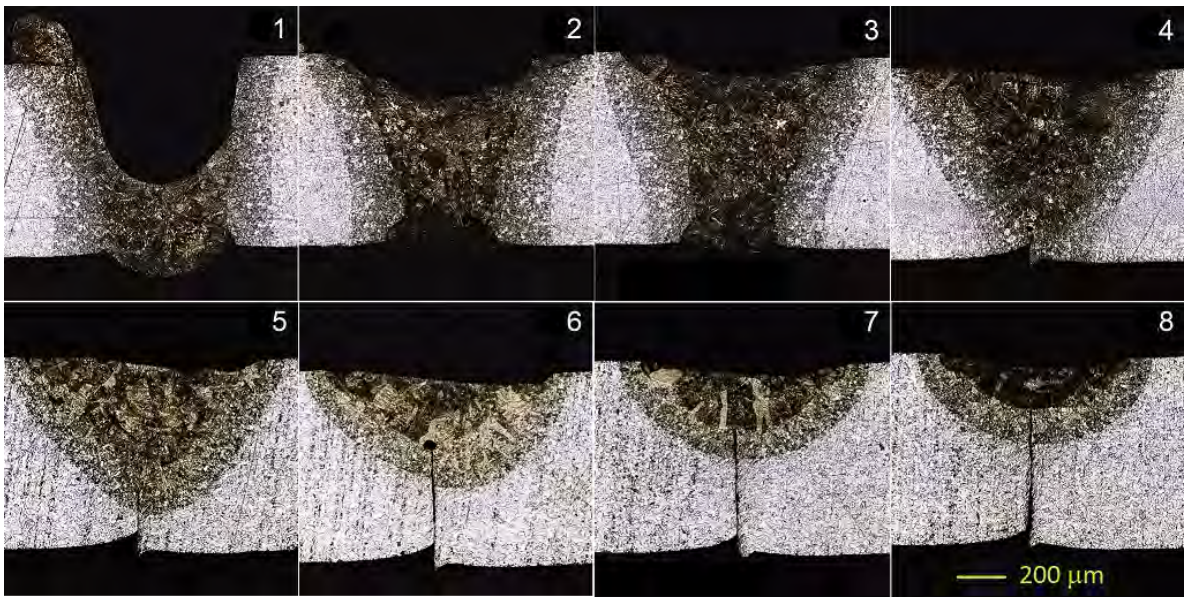

Fig. 1. Summary display of the cross-sections of all examined samples, welded with increasing pulse length (LEXT 5000, objective 20x)

3.2. Surface morphology

The surface data were collected from the selected area (4 x 4) mm^2 close to the weld start. 3D axonometric displays of the sample 3 top and bottom side were displayed in color mode on Fig 2. The occasional occurrence of droplets on the sample surfaces was detected, caused by higher surface power density. Periodic alternation of the peaks and valleys in the longitudinal direction was caused by the overlap of laser pulse spots (Fig 2a). The high of the root humping much alternated along measured section of the weld line. The individual peaks are more separated due to the narrower width of the fusion zone on the weld bottom side that caused smaller laser spots overlap (Fig 2b).

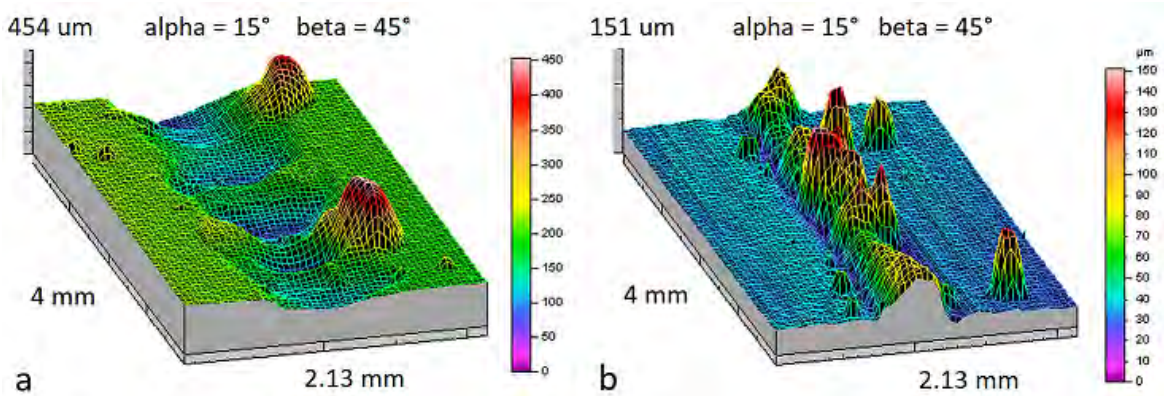

Fig. 2. (a) 3D axonometric display of the sample 3 top surface, scale 450 µm; (b) 3D axonometric display of the sample 3 bottom surface, scale 150 µm

3.3. Microstructure

Gradual evolution of the weld microstructure in about half the thickness of sample 3 in the horizontal direction from the base material (BM) through the heat-affected zone (HAZ) to the fusion zone (FZ) is shown on Fig 3. The partially transformed HAZ contains locally grains of BM, mixed with transformed α, acicular α´ grains and laths, the occurrence of which gradually increases towards the weld center (Fig 3a). The irregular structure of laths and needles in the HAZ softens towards the transition to the fusion zone (Fig 3b). Fig. 3c shows the structure of the edge part of the weld. The structure contains larger primary β grains formed from acicular and dendritic shapes, which are probably martensitic α´ phase.

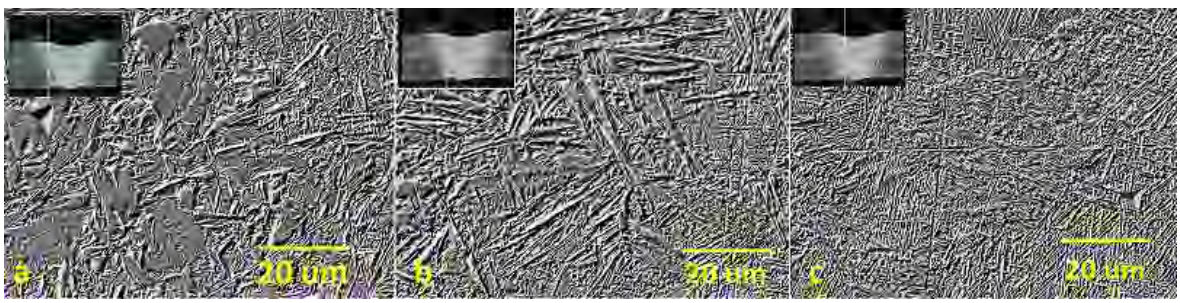

Fig. 3. Microstructure development of the sample 3 in half thickness: (a) transition between partially and fully transformed HAZ; (b) fully transformed HAZ; (c) fusion zone at the left part of the weld

A similar structure occurs in the vertical axis of the fusion zone, where certain differences in primary β grains shape, dimensions and orientation can be observed between the upper, central and bottom parts of it, which are caused by the different number of the repeated remelting during pulse overlap welding and a cooling rate (Fig 4). Elongated grains with the same orientation at the bottom part (Fig 4a) changed their shape to more equiaxed one in central part (Fig 4b) and reduced size towards upper surface (Fig 4c).

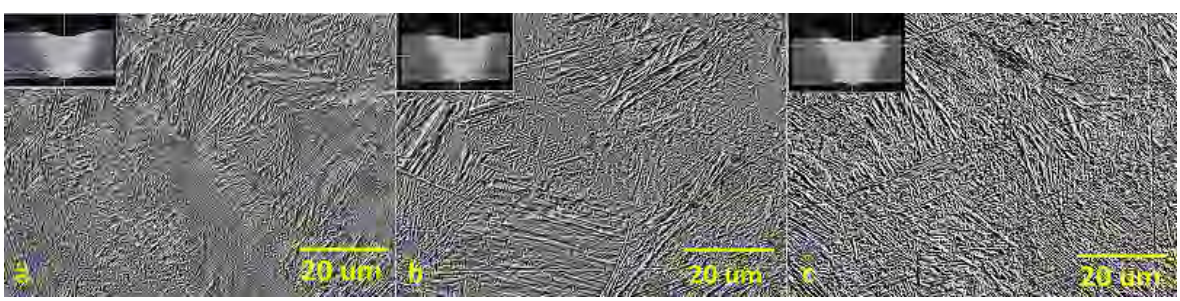

Fig. 4. Microstructure development of the sample 3 fusion zone in vertical axis: (a) a bottom part; (b) a central part; (c) an upper part

3.4. Numerical model

Temperatures profiles in the weld line at four consecutive times of the pulse application are displayed on Fig 5a. For instance, the surface point Y = 1.1 mm achieved maximum temperature 2598 °C (red line), after the next pulse applying, temperature exceed the melting value again up to 2220 °C (yellow line), after another pulse action the temperature increased to 1390 °C (cyan line) and the last pulse increased temperature to 870 °C, i.e. just below the Ti6Al4V transformation point (blue line).

Temperature history of the periodical heating and cooling in the selected node No. 600218 (mesh coordinates x = 0.04 mm, y = 2.12 mm and z = 0.12 mm) is displayed on Fig 5b. Achieved temperature above 1700°C and fast cooling to about 700 °C caused phase transformation in selected node even before impact of the laser beam intensity centre at time 0.468 s. Maximum temperature was reached close to 2470°C after actual pulse application at time 0.545 s. After it, post heating above the melting temperature (2020 °C) by the next pulse caused re-melting at time 0.622 s. The second next pulse heated the discussed node above transformation temperature to about 1480 °C in a time of 0.699 s.

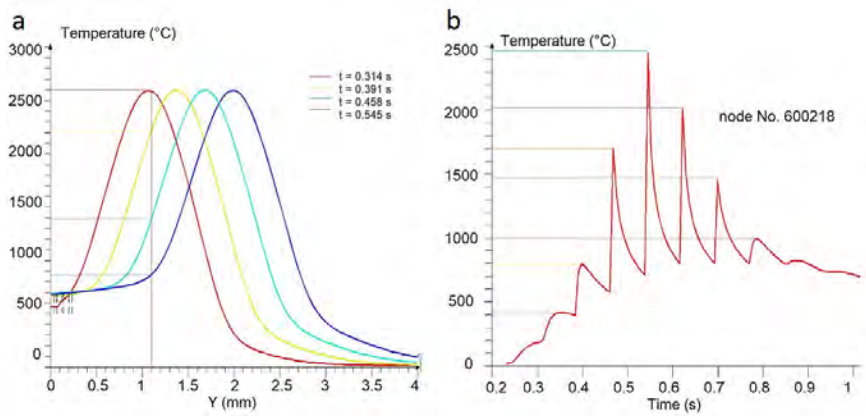

Fig. 5. (a) Temperature profile along the weld line for four consecutive pulses in times of 0.314 s to 0.545 s; (b) temperature history in the mesh node No. 600218 in depth 0.12 mm below the weld line between times 0.3 s and 1 s.

2D temperature field distributions in the plane Y = 2.12 mm at four consecutive times of the laser pulse actions are displayed on Fig 6. When pulse was applied in previous point in time of 0.468 s, melting occurred at small area, temperature above 1000 °C reached sample bottom part (Fig 6a). In time of 0.545 s laser pulse was applied (Fig 6b), red area indicates dimensions of FZ, yellow and cyan iso-surfaces define fully and partially transformed HAZ. FZ was partially melted again by the next pulse (time of 0.622 s), both HAZs were reheated above the transformation temperature (Fig 6c). Finally, temperature above 1000 °C was achieved in the whole FZ area in time of 0.699 s with values higher then 1200 °C in the central upper area (Fig 6d).

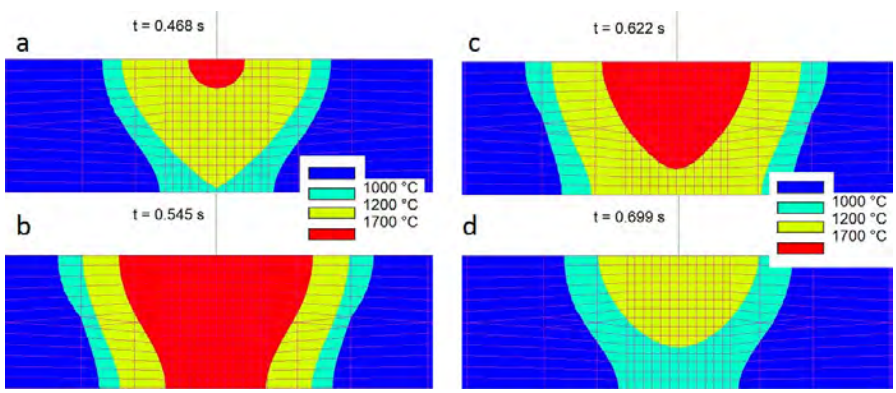

Fig. 6. Temperature field distribution in the plane Y = 2.12 mm in times of: (a) 0.468 s; (b) 0.545 s; (c) 0.622 s; (d) 0.699 s

3.5. Nano indentation

Matrix of the 17 nanohardness values in a horizontal and 8 values in a vertical direction was taken from the sample 3 cross-section with step of 100 µm. The average hardness value of the base material was found to be 2.86 GPa. The individual values varied from 2.33 GPa to 3.13 GPa. The coarse-grained fusion zone of the complete welded sample 3 possessed an average hardness of 4.25 GPa, varying from the local minimum 3.35 GPa to the local maximum 5.79 GPa. This means that the fusion zone is approximately 48 % harder than the base material. The heat-affected zone between the fusion zone boundary and the base material exhibited average hardness of 3.55 GPa of values from 2.88 GPa to 4.16 GPa. The nanohardness distribution in the measured area is shown as a 2D surface graph in Fig 7a.

In the case of reduced elastic modulus E_r values, there are smaller differences between values of the base material and the fusion zone. The average reduced modulus value for Ti6Al4V alloy is 136 GPa, from a minimal value 113 GPa to a maximum 157 GPa, which are occasionally observed across the measurement area. This may reflects the local inhomogeneity of the weld macrostructure (Fig 7b).

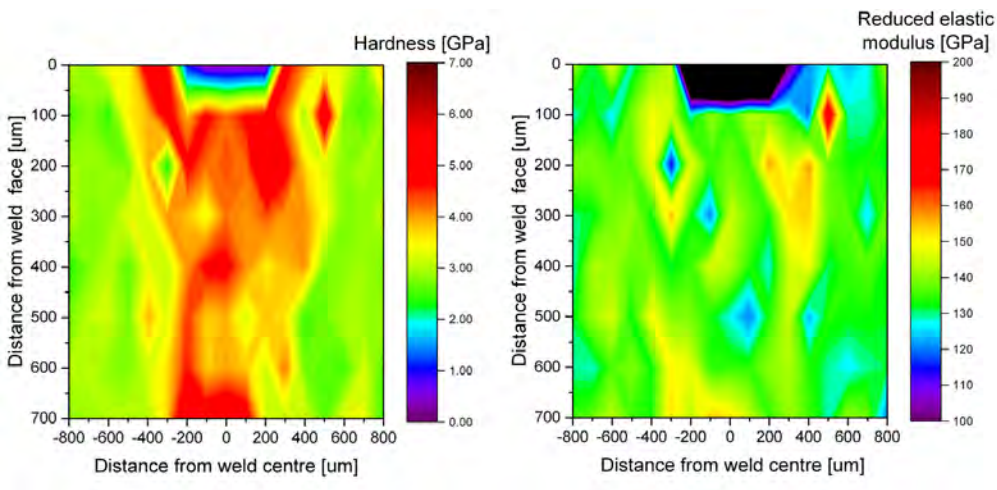

Fig. 7. (a) Nanohardness distribution in the cross section of the sample 3; (b) reduced elastic modulus distribution in the cross section of the sample 3

3.6. XRD analysis

Fig 8 shows the X-ray diffraction patterns obtained from a fusion zone central part of the sample 3. The structure was assigned as titanium with hexagonal close packed crystal structure (hcp) with Reference code 96-900-8518. According to Kumar et al. 2020, the lattice parameter of *α* and *α´* martensite is nearly same, so intensive peaks correspond to dominant *α*' can be seen in the spectra, especially plane intensity *α* (101), *α* (110) and *α* (002). List of peaks from ICDD database was compared with measured XRD spectra. It is observed that the relative intensity of the experimental joints is higher than database data at position 35.097°, corresponding to plane (100)α and 62.965° - plane (110)α, on the contrary, for positions 38.388°, 70.623° and 76.210° the relative intensity was found up to 3 times lower, two peaks above 80° fell below the noise limit. We have found a similar trend in the publication on heat treatment Ti6Al4V 5.5 mm (Beladi et al., 2014 or Xu et al., 2014).

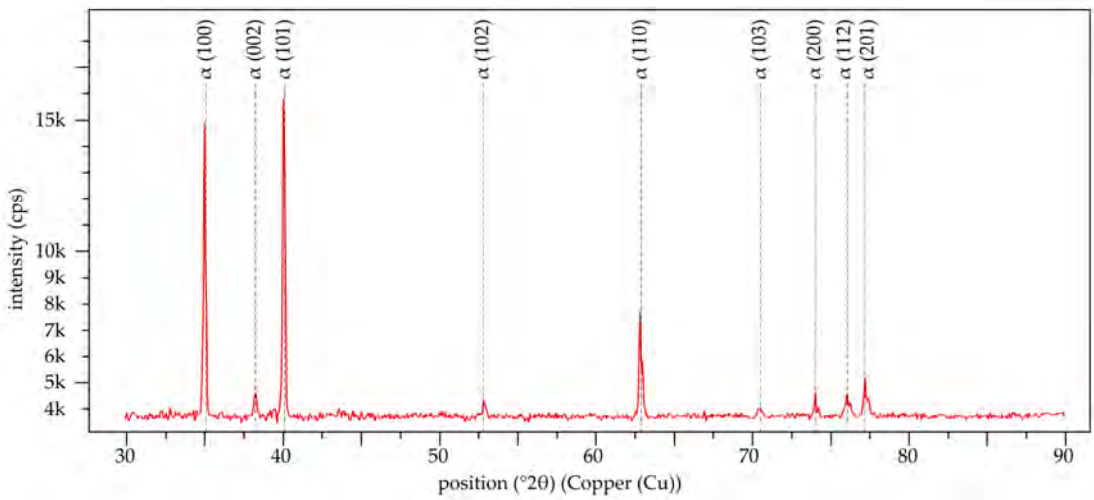

Fig. 8. X-ray diffraction patterns taken in the fusion zone centre of the completely welded sample 3

4. Conclusions

The optimal welding parameters of the Ti6Al4 sheets with a thickness of 0.8 mm by pulsed Nd:YAG laser were investigated for eight values of pulse length form 2.0 ms to 5.5 ms, keeping other parameters constant (energy E = 5.03 J, frequency f = 13 Hz, scanning velocity v = 3 mm·s^{-1}).

Microscopy images of the samples cross sections revealed decreasing depth of penetration with increasing pulse length, close to the optimal X – shape weld was achieved with pulse length t_p = 3 ms.

The microstructure of its cross section different areas was displayed, and it was concluded that they contain α/α' phases with different morphology of α' martensite (described as acicular or dendritic) and laths of transformed α. In the fusion zone, martensite predominates, in the heat-affected region, proportion of martensite gradually decreased and transformed α and then primary β contains increased.

Output from numerical model illustrated preheating, re-melting and post-heating of each point of the laser pulse application. The measurement of nanohardness also confirmed the predominant occurrence of martensite in the fusion zone and its gradual decrease in favor of the transformed α phase towards the base material.

The values of the reduced modulus of elasticity were slightly higher than the tabulated values for the base material.

The results of XRD (X-ray diffraction analysis) demonstrated the presence of a hexagonal crystal lattice of α/α' phases with unproven β phase peaks.

Acknowledgements

Authors gratefully acknowledge the support of the Ministry of Education, Youth and Sports of the Czech Republic project LM 2023032.

References

Beladi, H., Chao, Q., Rohrer, G. S., 2014. Variant selection and intervariant crystallographic planes distribution in martensite in a Ti–6Al–4V alloy, Acta Mater 80, p. 481.

Chludzinski, M., dosSantos, R.E., Churiaque, C., Ortega-Iguña, M., Sánchez-Amaya, J.M., 2021. Pulsed Laser Welding Applied to Metallic Materials—A Material Approach. Metals 11, p. 2.

Chmelíčková, H., Hiklová, H., Václavek, L., Tomáštík, J., Čtvrtlík, R., 2019. Characterization of titanium laser welds, Acta Polytechnica CTU Proceedings 27, p. 145.

Kabir, A. S. H., Cao, X., Medraj, M., Wanjara, P., Cuddy, J., Birur, A., 2010. "Effect of Welding Speed and Defocusing Distance on the Quality of Laser Welded Ti-6Al-4V, " Materials Science & Technology Conference and Exhibition. Houston, Texas, p. 2795.

Kumar, B., Kebede, D., Bag, S., 2018. Microstructure evolution in thin sheet laser welding of titanium alloy, International Journal of Mechatronics and Manufacturing Systems 11, p. 203.

Kumar, B., Bag, S., Paul, C.P., Das, C.R., Ravikumar, R., Bindra, K.S., 2020. Influence of the mode of laser welding parameters on microstructural morphology in thin sheet Ti6Al4V alloy. Optics & Laser Technology 131, p. 12.

Kumar, Ch., Das, M., Paul, C. P., Bindra, K. S., 2018. Comparison of bead shape, microstructure and mechanical properties of fiber laser beam welding of 2 mm thick plates of Ti-6Al-4V alloy. Optics & Laser Technology 105, p. 320.

Lapšanská, H., Havelková, M., Chmelíčková, H., 2010. "FEM simulation of pulsed laser seam welding, " 48th International Scientific Conference EAN, Velké Losiny, Czech Republic, p. 221.

Lisiecki, A., 2012. Laser welding of titanium alloy Ti6Al4V using a disk laser. Machines. Technologies. Materials 7, p. 53.

Sibillano, T., Rizzi, D., Ancona, A., Sadules-Rodil, S., Rodriguez Nieto, J. R., Chmelíčková, H., Šebestová, H., 2012. Spectroscopic monitoring of penetration depth in CO_2, Nd:YAG and fibre laser welding processes, Journal of Materials Processing Technology 212 (4), p. 911.

Xu, PQ., Li, L., Zhang, Ch. (S.), 2014. Microstructure characterization of laser welded Ti-6Al-4V fusion zones, Materials Characterization 87, p. 180.